

Raman scattering study of lattice and magnetic excitations in CrAsK. Sen¹,* Y. Yao, R. Heid, A. Omoumi, F. Hardy, K. Willa, M. Merz, A. A. Haghighirad, and M. Le Tacon¹
Institute for Solid State Physics, Karlsruhe Institute of Technology, D-76344, Eggenstein-Leopoldshafen, Germany

(Received 3 May 2019; revised manuscript received 15 July 2019; published 4 September 2019)

We report on the lattice and spin dynamics in monpnictide CrAs using polarized Raman scattering. This system exhibits a first-order magnetostructural phase transition at $T_N \sim 265$ K, below which the magnetic moments of Cr form an incommensurate double helical magnetic structure while the unit-cell volume abruptly expands. Across the transition, the frequencies of the fully symmetric A_g phonons strongly renormalize, which along with the results of first-principles calculations suggests the presence of a sizeable coupling of the phonons to the magnetic degrees of freedom in this compound. In addition, we observe two broad modes at around 350 and 1700 cm^{-1} in the magnetic phase, which we associate with two-magnon Raman scattering. This work provides one of the few examples of magnetic Raman scattering from a noncollinear magnet.

DOI: [10.1103/PhysRevB.100.104301](https://doi.org/10.1103/PhysRevB.100.104301)**I. INTRODUCTION**

Transition-metal pnictides have been widely studied in recent years, particularly following the discovery of high-temperature superconductivity in the Fe-based compounds [1–4]. This has also revived interest in related compounds, including monpnictides such as MnAs, which has long been known as a magnetocaloric material [5]. This paper focuses on another representative of this family of compounds, CrAs, a semimetal which undergoes a first-order phase transition from a paramagnetic (PM) state to a noncollinear magnetic state below $T_N \approx 265$ K at ambient pressure [6–9]. At T_N , it exhibits a giant structural anomaly which involves a large expansion of the crystallographic b axis by $\sim 3.9\%$ and the unit-cell volume by $\sim 2.2\%$, while the space group of $Pnma$ remains unaltered [10].

The itinerant character and the complex antiferromagnetic (AF) magnetic structure of CrAs attracted some attention in the early 1970s [6,7,9,11,12]. In particular, the magnetic structure was investigated in great detail, revealing a large magnetic moment of Cr ($\sim 1.73 \mu_B$ at 1.5 K) lying in the ab crystallographic plane and forming a double helical structure with the propagating wave vector $(0, 0, 0.356)$ in the reciprocal lattice unit [8]. Studies on single crystals have overall been limited by the fact that pristine compound tends to break upon thermal cycling, which is due to the large magnetostriction effect across T_N . Yet, the interest for this material has recently been revived for several reasons, the first of them being the discovery of superconductivity (SC) under pressure in this system. When the helical magnetic order is suppressed under hydrostatic pressure, bulk SC emerges and displays a domelike pressure dependence with a maximum SC transition temperature of $T_c \approx 2$ K [13–15], making this system the first known “Cr-based” superconductor.

While the domelike pressure dependence of T_c is strongly reminiscent of unconventional superconductors, CrAs ex-

hibits several other features that are typically encountered in correlated materials. For instance, in the PM phase above T_N , the magnetic susceptibility increases linearly with temperature up to 700 K [16], similar to what is generically found in iron-based superconductors and often regarded as an evidence for finite AF fluctuations in the PM phase [14].

Below T_N , the electrical resistance drops abruptly and follows a Fermi-liquid-like T^2 behavior [14,17,18], suggesting a substantial modification of the Fermi surface across the magnetostructural transition. Strong deviations from this Fermi-liquid behavior are observed, as the long-range magnetic order entirely vanishes above a critical pressure of $p_c \approx 10$ kbar, and are accompanied with a sizeable enhancement of the electronic effective mass close to p_c (inferred from specific heat measurements). This has been interpreted as a signature of quantum criticality, which in turn suggests an unconventional superconducting pairing mechanism [17]. Furthermore, it has been argued that the AF spin fluctuations that are present at ambient pressure are critically enhanced at $\approx p_c$ [14]. Around this pressure, quasilinear and nonsaturating magnetoresistance have been reported and are associated with the singular electronic band structure of this material [19]. Above p_c , nuclear quadrupole resonance experiments revealed the presence of substantial magnetic fluctuations [20], whereas the electrical resistivity depends quasilinearly on the temperature [17]. Already at ambient pressure, the very large magnetostriction effect at T_N indicates a strong coupling of the lattice to the underlying static magnetic order. To the best of our knowledge, however, no experimental study of the lattice dynamics of CrAs nor of its coupling to magnetism has been reported.

Here, we address this topic and present a comprehensive Raman scattering study of lattice dynamics and magnetic excitations in CrAs as a function of temperature at ambient pressure. Raman spectroscopy is an ideal tool to simultaneously probe zone-center lattice (phonons) and magnetic (single and bimagnons) excitations in correlated systems [21]. We reveal anomalously large renormalization (both in frequency and linewidth) of the phonons of A_g symmetry across the magnetostructural transition, as well as some excitations

*kaushik.sen@kit.edu

†matthieu.letacon@kit.edu

below T_N that we associate with two-magnon Raman scattering. Detailed comparison with first-principles calculations indicates the presence of a large spin-phonon coupling in CrAs.

The paper is organized as follows. Section II comprises details on the crystal growth, structural and magnetic characterization, Raman scattering measurements, and the corresponding data analyses. In Sec. III, we present the details of the first-principles calculations. Experimental results and discussion are presented in Secs. IV and V, respectively.

II. EXPERIMENT

A. Crystal growth and structural characterization

Crystals of CrAs were grown from Sn flux. First, polycrystalline CrAs was prepared from the high-purity elements chromium (99.99%, Alfa Aesar) and arsenic (99.999%, ChemPUR) by weighing the stoichiometric mixture of the elements, which was subsequently evacuated and sealed in a quartz ampoule. The latter was heated at 700 °C for 20 h and then cooled to room temperature (RT) at a rate of 50 °C/h. The product was ground in argon atmosphere in a glove box, and the phase purity was checked by powder x-ray diffraction. CrAs and pieces of Sn with molar ratio of CrAs:Sn $\approx 1 : 10$ were added to an alumina crucible and placed in a quartz ampoule which was evacuated at 10^{-5} mbar and sealed. The quartz ampoule was heated to 650 °C and kept there for 10 h, then heated to 900 °C with a dwell time of 5 h, and slowly cooled to 685 °C in 7 days. At this temperature, the excess of Sn was centrifuged and the remaining Sn flux was washed off the CrAs single crystals using a 30% HNO₃ solution. Large crystals with shiny facets and dimensions up to $5 \times 0.5 \times 0.7$ mm [see Fig. 1(a)] were obtained. The single crystals have habitus that look similar to a hexagonal system. This can be explained by the fact that CrAs undergoes a second-order phase transition below 1173 K from a NiAs-type (hexagonal) structure to a MnP-type (orthorhombic) structure [12,22].

Temperature-dependent x-ray diffraction data on CrAs single crystals were collected between 85 K and room temperature on a STOE imaging plate diffraction system (IPDS-2T) using Mo $K\alpha$ radiation. All accessible symmetry-equivalent reflections (≈ 5000) were measured up to a maximum angle of $2\theta = 65^\circ$.

The data were corrected for Lorentz, polarization, extinction, and absorption effects. Using SHELXL [23] and JANA2006 [24], around 160 averaged symmetry-independent reflections ($I > 2\sigma$) have been included for the respective refinements in space group $Pnma$. The refinement converged quite well and shows excellent weighted reliability factors (wR_2), which for all temperatures are around 4%. The temperature-dependent lattice parameters, bond angles, and bond distances were derived from the atomic positions of Cr and As. They are shown in Figs. 1(d), 6(b), 6(c), and 6(d), respectively. In addition, we listed the structural parameters at room temperature and 95 K in Appendix A.

B. Magnetization measurements

The magnetic susceptibility of CrAs was obtained by gluing a single crystal with a mass of ≈ 12 mg to a polyether

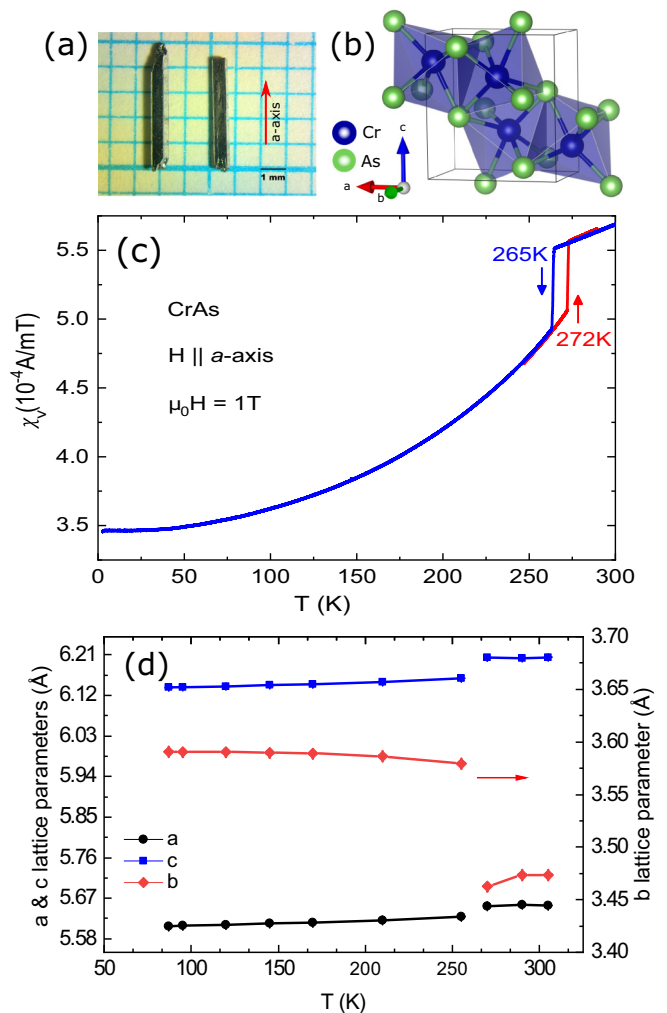


FIG. 1. (a) Typical size and morphology of as-grown single crystals of CrAs. The crystallographic a axis is marked with respect to the crystals. (b) Crystallographic unit cell of orthorhombic CrAs (space group $Pnma$, no. 62). (c) Magnetic volume susceptibility (χ_v) of CrAs as a function of temperature during cooling and warming. The large drop in χ_v at 265 K during cooling marks the first-order magnetostructural transition. (d) a -, b -, and c -axis lattice parameters as functions of temperature, which were determined from single-crystal x-ray diffraction.

ether ketone substrate and mounting it into a Quantum Design physical properties measurement system. Measurements were performed with the standard vibrating sample magnetometer option at a field of 1 T along the crystallographic a axis. The measured susceptibility, plotted in Fig. 1(c), shows a sharp jump at the magnetic transition with a width of < 1.5 K. We observe a pronounced hysteresis, as expected for a first-order phase transition, with transition temperatures of 265 K upon cooling and 272 K on warming.

C. Raman scattering

Raman scattering experiments were performed in backscattering geometry using a Jobin-Yvon LabRAM HR evolution spectrometer. A He-Ne laser ($\lambda = 632.8$ nm) was focused

onto the facets of the single crystals [see Fig. 1(a)] through a $50\times$ microscope objective. We used a laser power of ≈ 1 mW and a laser spot size of ≈ 5 μm in diameter to limit laser-induced heating. The scattered photons are dispersed by a grating with 1800 (respectively 600) grooves/mm and recorded with a Peltier-cooled CCD detector. The total energy resolution of the spectrometer is 0.6 (resp. 1.8) cm^{-1} , which was determined from the direct measurements of resolution limited Ne emission lines. Temperature-dependent Raman spectra were acquired by cooling the sample in a He-flow cryostat. The Raman susceptibility χ'' was obtained by correcting the recorded Raman spectra from the Bose factor, $1 + n(\omega, T)$.

The high-resolution mode was used to analyze the phonons, whereas the magnetic excitation spectra were recorded using the low-resolution mode, which maximizes the throughput of the Raman spectrometer. Phonon frequencies and linewidths were obtained by fitting the peaks using Voigt profiles (intrinsic Lorentzian line shapes convoluted with the Gaussian experimental resolution).

From a group theoretical analysis of the orthorhombic structure of CrAs (space group $Pnma$ and point group D_{2h} , both Cr and As occupy $4c$ Wyckoff positions) [11,25,26], 21 optical phonon modes at the zone center are expected. Among them 12 are Raman active with A_g (four modes), B_{1g} (two), B_{2g} (four), and B_{3g} (two) symmetries.

The weak intensity of the B_{1g} and B_{2g} modes in crossed polarization (see in Appendix B) did not allow us to carry out their systematic temperature dependence. For this reason, in this paper we have restricted ourselves to a study of the fully symmetric A_g modes, which were probed by keeping the incoming and scattered photon polarizations parallel to the crystallographic a axis of the sample (XX configuration in Porto's notation), irrespective of the facet of the crystal on which they are measured (see in Appendix C).

III. LATTICE DYNAMICS CALCULATION WITH DENSITY FUNCTIONAL THEORY

Density functional calculations were carried out for CrAs using the mixed-basis pseudopotential method [27]. We used norm-conserving pseudopotentials with nonlinear core corrections and included the semicore states Cr-3s, Cr-3p, and As-4s in the valence space. The mixed-basis approach describes valence states with a combination of plane waves and local functions. The latter allow an efficient description of more localized components of the valence states. For CrAs, we used plane waves up to a kinetic energy of 24 Ry (326.5 eV), augmented by local functions of s , p , and d type at the Cr sites. For the exchange-correlation functional, we employed the Perdew-Burke-Ernzerhof (PBE) parameterization of the generalized gradient approximation (GGA) [28], and Brillouin zone integrations were performed with a $8 \times 12 \times 8$ orthorhombic k -point grid in conjunction with a Gaussian smearing of 0.1 eV.

Zone-centered phonons were calculated using the linear response or density functional perturbation theory implemented in the mixed-basis scheme [29]. Internal structural parameters were relaxed prior to the phonon calculations. To analyze the effect of purely structural changes at the phase transition

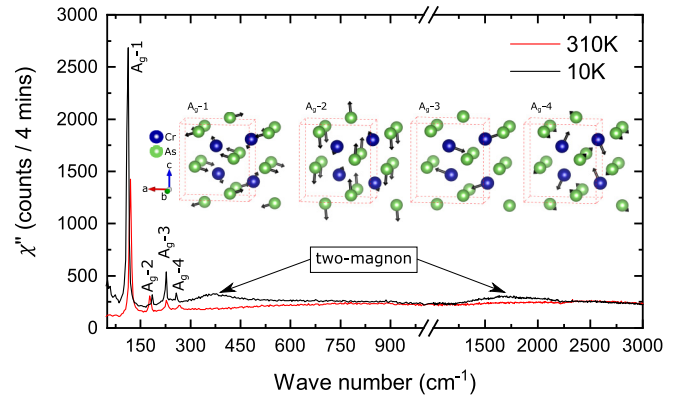


FIG. 2. Representative Raman spectra (χ'') at two temperatures below (10 K) and above (310 K) $T_N = 265$ K in XX geometry, which probes the lattice dynamics and magnetic excitations of A_g symmetry. The sharp peaks at low energy are four phonon modes of A_g symmetry. The two broad modes at higher energy originate from magnetic Raman scattering, which we attribute to two-magnon modes. Insets show the atomic displacement patterns of the four phonon modes, which were determined from the DFT-based lattice dynamics calculations.

on the Raman modes, we performed calculations for two sets of experimental structural parameters corresponding to room temperature and 95 K (see in Appendix A), respectively, after internal relaxation of the atomic positions. To study the effect of magnetism on the structure and on the lattice dynamics, we performed additional spin-polarized calculations with both collinear ferromagnetic (FM) and antiferromagnetic structures. The AF order involves the antiparallel alignment of the neighboring Cr spins within a unit cell along both in-plane and out-of-plane directions.

The obtained atomic displacement patterns of these individual modes are depicted in the inset of Fig. 2. The calculated eigenfrequencies of the A_g Raman modes are shown in Figs. 5(a) and 5(b).

IV. EXPERIMENTAL RESULTS

A. Raman-active phonons

In Fig. 2, we show the typical Raman response of CrAs at two temperatures above and below the magnetostructural transition. At 310 K, all four expected A_g modes were detected and will be referred to as A_g -1 (118.9 cm^{-1}), A_g -2 (178.8 cm^{-1}), A_g -3 (227.6 cm^{-1}) and A_g -4 (265.0 cm^{-1}), respectively. The Raman spectra are dominated by the A_g -1 mode, which is almost an order of magnitude more intense than any of the other three modes. All the modes could be fitted with Voigt profiles, and no Fano asymmetry was detected.

As already evident from the data displayed in Fig. 2, the four Raman modes are strongly renormalized across T_N . In Figs. 3(a)–3(h), we present a more detailed temperature dependence of the frequency and linewidth (FWHM) of all the A_g modes.

The temperature dependence of the phonon frequencies and linewidths in crystals is generally governed by anharmonic effects. Phonons are expected to harden continuously as the temperature decreases and the lattice contracts,

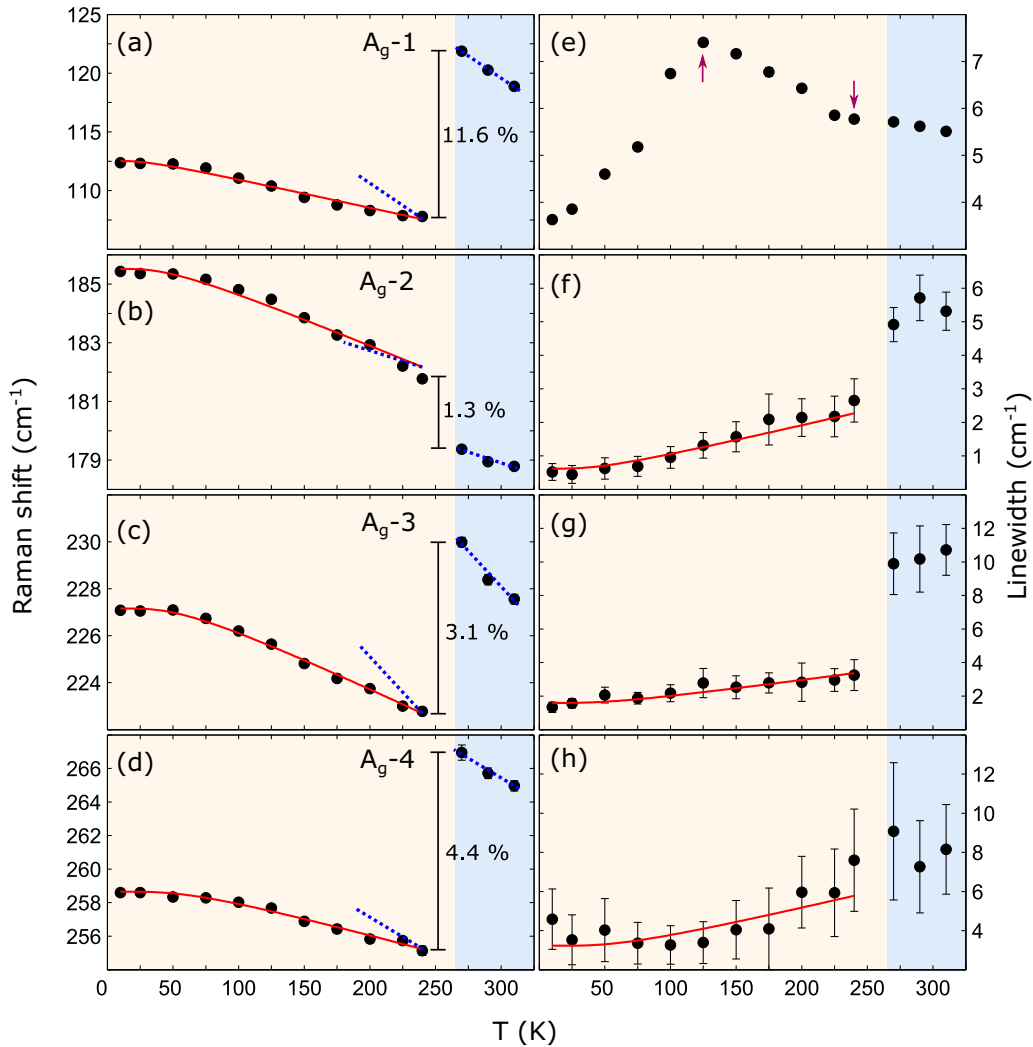


FIG. 3. (a)–(d) Raman shift as a function of temperature for the four A_g phonon modes. (e)–(h) The corresponding linewidths as functions of temperature. For small uncertainty the error bars are hidden behind the symbols. The solid lines (red) are the best fits to the data with the Klemens decay model [30,31]. The dotted lines in (a)–(d) in low-temperature phase ($< T_N = 265$ K) are parallel to the corresponding lines which go through the data in the high-temperature phase. The down arrow in Fig. 3(e) marks the onset temperature near T_N , below which the linewidth starts broaden upon cooling to 125 K (indicated by the up arrow).

whereas their linewidths, inversely proportional to the modes' lifetimes, decreases with decreasing phonon population and phonon-phonon scattering. We further fitted (solid lines in Fig. 3) the regular temperature dependence of the phonon frequencies and linewidths using the symmetric anharmonic phonon decay model (Klemens model), in which an optical phonon decays into two acoustic phonons of opposite momenta [30,31].

This trend for the frequency is qualitatively followed for all modes above and below T_N . Across T_N , however, a sudden renormalization of the phonon frequencies is observed, as expected from the first-order nature of the magnetostructural transition. While the A_g -1, A_g -3 and A_g -4 modes significantly soften below the transition, the A_g -2 mode exhibits a small hardening ($\Delta\omega/\omega = (\omega_{T < T_N} - \omega_{T > T_N})/\omega_{T > T_N} = 1.3\%$). We note here that the softening of the A_g -1 mode is particularly strong, with a relative frequency change of $\Delta\omega/\omega = -11.6\%$ across T_N . This exceeds the expectations from Grüneisen's law, which relates the phonon frequencies and the unit-cell

volume by $\Delta\omega_i/\omega_i = -\gamma_i\Delta V/V$. For the A_g -1 mode, we get the Grüneisen parameter as $\gamma_{A_g-1} \approx 5.3$, a value which is significantly larger than the typical values (2–3) for Grüneisen parameters [32].

It is also interesting to compare the rate of change of the phonon frequency above and below T_N . To this aim, we added dotted lines to Figs. 3(a)–3(d) at $< T_N$, representing the slopes $d\omega/dT$ measured between room temperature and T_N . Except for A_g -2, the rate of hardening of all phonons strongly slows down in the magnetic phase. Interestingly, while the hardening of 2–4 cm^{-1} for all the modes between T_N and the base temperature is rather normal, the changes of the same amplitude within only 30 K between room temperature and T_N appear remarkable. This anomalously large temperature dependence indicates an unusually large lattice anharmonicity in the PM phase.

As far as the linewidths are concerned [Figs. 3(e)–3(h)], the very small residual width of the phonons (0.5 cm^{-1} FWHM for the A_g -2 mode and 2–4 cm^{-1} for the others, including

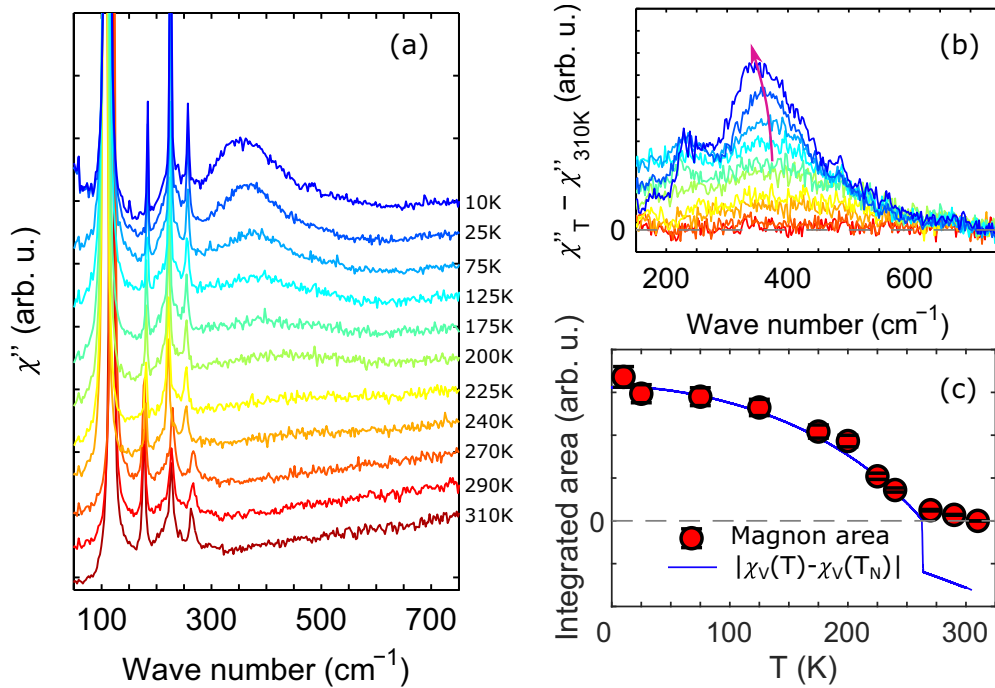


FIG. 4. (a) Normalized Raman response (χ'') as a function of temperature. (b) $\Delta\chi''(T) = \chi''(T) - \chi''(310\text{ K})$ at several temperatures. Prior to the calculation of $\Delta\chi''(T)$, we first subtracted the phonon contributions from the individual spectrum. The arrow marks the apparent softening of the most intense mode. (c) Integrated area under the curves in (b) as a function of temperature. The solid lines through the data are evaluated from χ_v (cooling curve), as described in the text.

the modes of B_{1g} and B_{2g} symmetries) at base temperature confirms the high quality of the investigated single crystals, which is in accordance with our x-ray diffraction (XRD) results. In addition, the lack of Fano asymmetry in the line shape of these modes indicates weak coupling of these phonons to any electronic continuum in CrAs.

Except for the A_g-4 mode, which has an extremely weak intensity to reliably determine its linewidth, the temperature dependences of the linewidths of the other phonons are found to be remarkable. The A_g-2 and A_g-3 modes generally narrow upon cooling as expected, but their FWHMs abruptly drop by more than 50% across T_N . To our surprise, the lineshape of A_g-1 does not seem to be affected by the magnetostructural transition. Moreover, slightly below T_N , it starts to anomalously broaden upon cooling, a trend that we observed down to $T \approx 125\text{ K}$; however, it rapidly narrows to the base temperature upon further cooling. Before we discuss the origin of the anomalous phonon behavior of A_g-1 in Sec. V, we briefly mention another set of Raman-active excitations that rises below T_N .

B. Evidence of magnetic Raman scattering

As seen already in the overview presented in Fig. 2, two distinct broad features at ≈ 350 and 1700 cm^{-1} that were not present at 310 K are visible at 10 K. In Fig. 4(a), we present a detailed temperature dependence of the lower energy mode, as well as in Fig. 4(b), the temperature-dependent part of the Raman response $\Delta\chi''(T) = \chi''(T) - \chi''(310\text{ K})$ in the same temperature range after subtraction of the phonon contributions. This clearly indicates that the 350-cm^{-1} feature

appears just below T_N narrows and rapidly grows in amplitude as the temperature is further reduced.

To be more quantitative, we show in Fig. 4(c) the spectral weight of $\Delta\chi''$ (integrated between 150 and 750 cm^{-1}) as a function of temperature. The integrated intensity appears to saturate below $\approx 80\text{ K}$. Apparently, such a temperature dependence is closely linked to the magnetic susceptibility (χ_v) shown in Fig. 1(c). The solid line in Fig. 4(c) corresponds to $|\chi_v(T) - \chi_v(T_N)|$, which perfectly reproduces the temperature dependence of the 350-cm^{-1} feature's intensity. This naturally suggests a magnetic origin of this excitation.

We finally note that at the lowest temperatures, when the 350-cm^{-1} mode becomes sufficiently narrow, an additional excitation can be resolved at around $\approx 230\text{ cm}^{-1}$, which is below the very sharp A_g-3 mode. All these features are completely absent from the Raman response measured in crossed polarization (one along the a axis and the other in the bc plane, see Appendix B). This is found to be consistent with expectations from the analysis of the Fleury-Loudon magnetic light-scattering Hamiltonian (see Appendix D).

V. DISCUSSION

A. Phonon renormalization across T_N

As described in Sec. IV A, the Raman-active phonons of CrAs are strongly renormalized across the first-order magnetostructural transition. To gain more insight, we have estimated the expected changes in the phonon frequencies using first-principles calculations (Sec. III) constrained to the lattice parameters, which were determined experimentally at

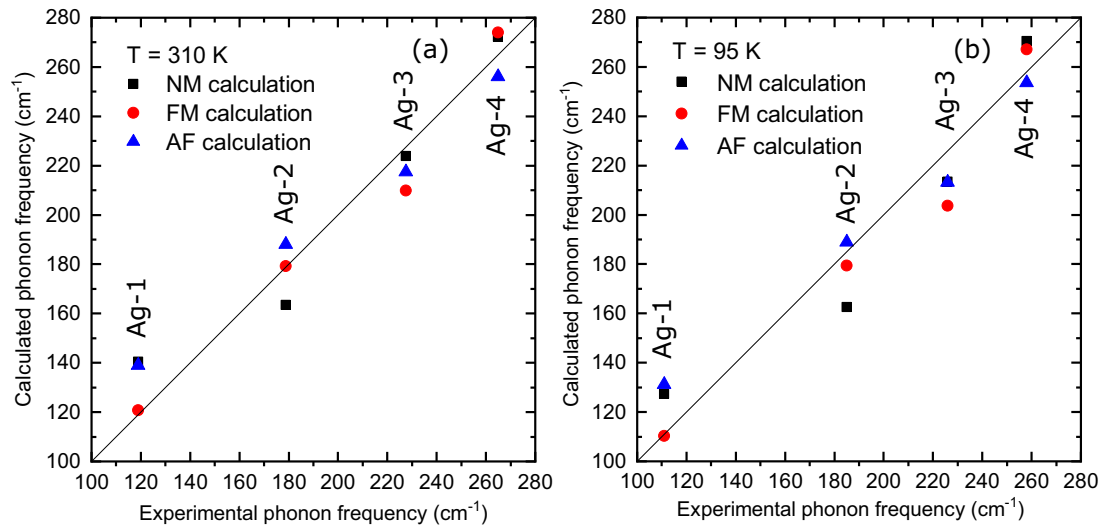


FIG. 5. Calculated phonon frequencies in nonmagnetic (NM), ferromagnetic (FM), and antiferromagnetic (AF) environments are plotted vs the experimental phonon frequencies at (a) 310 and (b) 95 K. The straight lines through the data have slopes equal to 1, which means data points fall on these lines if the experimental and calculated phonon frequencies are equal.

room temperature and at 95 K $\ll T_N$ (see Appendix A). We first carried out the calculations without considering the long-range magnetic order of the system, which was taken into account in a second step.

In Fig. 5, we compare the measured and calculated phonon frequencies in CrAs at 310 and 95 K. At both temperatures, significant differences between the theoretical and experimental frequencies are observed. A good agreement ($< 5\%$) is found for the A_g-3 and A_g-4 modes, whereas sizeable deviations from the experimental values are found for the A_g-1 ($\sim 15\% - 18\%$ off depending on the temperature) and A_g-2 ($\sim 8\% - 10\%$ off) modes.

To understand the origin of this discrepancy, it is instructive to compare the experimentally determined bond lengths and angles between the atoms in the unit cell with the calculated ones. Figures 6(c) and 6(d) reveal that at both temperatures most bond lengths agree within $\approx \pm 2\%$ with the experimental values. However, a noticeable discrepancy concerns the Cr-Cr bond B6 [marked in Fig. 6(a)], which is 5% too short in the calculation. Similarly, it underestimates the Cr-As-Cr angle A1 [denoted in Fig. 6(a)] by 3.16° . Furthermore, the analysis of the eigendisplacements of the A_g-1 and A_g-2 modes reveals that these are the phonons which give rise to the largest modulation of the Cr-As-Cr angle A1, which directly relates to the dominant magnetic exchange path [J_{c2} in Fig. 7(c)]. This in turn suggests that the inclusion of magnetism in the calculation is necessary to accurately account for the lattice dynamics in CrAs.

Performing phonon calculations with explicit inclusion of the actual double helical magnetic structure is beyond the scope of the present paper and will be the subject of subsequent theoretical studies.

To simply evaluate the impact of magnetism on the structural parameters and on the phonon frequencies, we have imposed FM and AF orders, relaxed the atomic positions in the unit cell, and calculated the frequencies of the Raman phonons. In agreement with a previous study [33], we find that the GGA functional significantly overestimates the magnetic

moment in CrAs. We obtained $2.4 (\sim 2.3) \mu_B/\text{Cr}$ above and below T_N for the FM (AF) case.

From a structural point of view, the inclusion of magnetism systematically improves the agreement between the calculated bond lengths and angles with the experimentally determined ones. As far as the bond lengths are concerned, the agreement is particularly good when considering AF order, while the FM order induces deviations to the experimental case opposite to that obtained for the nonmagnetic (NM) case. Indeed, as seen in Figs. 6(c) and 6(d), bond lengths that tended to be underestimated in the NM calculations are now slightly overestimated and vice versa. The Cr-As-Cr angles A2 and A4 are marginally affected by magnetism, opposite to A1 and A3 on which it has a much more dramatic effect. The FM calculation significantly overestimates A1, which is slightly underestimated by the AF calculation. The opposite trend is seen for A3, underestimated in the FM case, overestimated in the AF one. In either case, however, the agreement between FM/AF calculations and experiment is better than that of the NM calculation.

Consequently, the calculated phonon frequencies are generally found to be in better agreement with the experiment when including magnetism. FM has only little effect on A_g-4 , while A_g-1 , A_g-2 , and A_g-3 are strongly renormalized [see in Figs. 5(a) and 5(b)]. The former two are then in excellent agreement with the experiment (within $\approx \pm 3\%$). The trend is a bit different for the AF calculation that mostly affects the A_g-2 and A_g-4 modes, leaving A_g-1 essentially unmodified with respect to the NM case.

The detail of the interplay between the structural and magnetic degrees of freedom is certainly complex, but qualitatively we note that the inclusion of magnetism in the first-principles calculation has the strongest impact on the structural degrees of freedom that modulate exchange paths J_{c2} (AF) and J_{c1} (FM), which in turn dramatically affect the phonon frequencies. This demonstrates a significant coupling between spin and lattice degrees of freedom, and interestingly, this conclusion is valid both below and above the

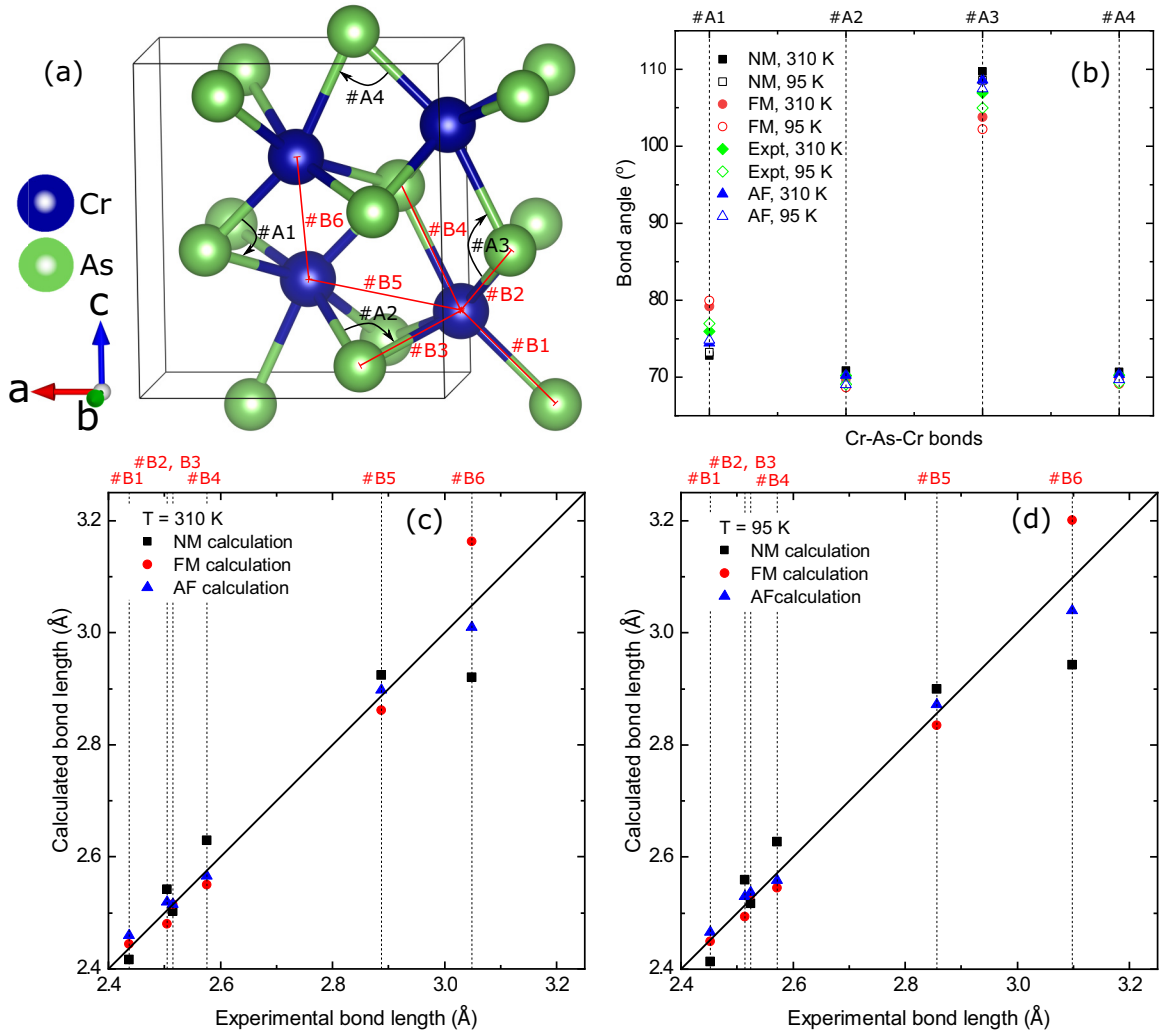


FIG. 6. (a) A sketch labeling the interatomic distances and Cr-As-Cr bond angles. (b) Comparison of the experimental bond angles with the calculations at 310 and 95 K in nonmagnetic (NM), ferromagnetic (FM), and antiferromagnetic (AF) cases. (c) Comparison of the interatomic distances at 310 K with the calculations. (d) The corresponding plot at 95 K.

magnetic transition. This is strongly reminiscent of the case of iron-based superconductors [34,35], in which the phonon frequencies and dispersion calculations agree best with the experiment when including magnetic order, even in the PM phase. We can finally expect that taking into consideration the actual double helical magnetic structure, which compromises between FM and AF interactions but is currently beyond our computational capabilities for lattice dynamic calculations, will yield the best agreement with the experiment.

We end this part of the discussion by noting that even in the nonmagnetic calculation, the relative change $\Delta\omega/\omega = (\omega_{95\text{K}} - \omega_{310\text{K}})/\omega_{310\text{K}}$ of the phonon frequencies is already well captured (not shown). In other words, even if magnetism must be included to correctly reproduce the phonon frequencies, the large Grüneisen parameter of the A_g-1 mode does not have a magnetic origin. Furthermore, our investigations reveal that this mode actually corresponds to the branch that gets completely soft at the zone boundary (M point) of the high-temperature hexagonal unit cell, when the phase transition to the orthorhombic phase takes place at 1173 K (this M point is then backfolded to the zone center). The amplitude

of the structural orthorhombicity, defined as $c/b (= \sqrt{3})$ in the hexagonal phase), increases down to T_N and suddenly changes its sign below the transition. The low-temperature structure is energetically very close to the hexagonal phase, which naturally affects the soft branch to which the A_g-1 mode belongs. The situation is very close to that of MnAs, which, however, goes back to the hexagonal phase at low-temperature and is also predicted to exhibit a large spin-phonon interaction [36].

B. Impact of spin-phonon coupling on phonon lifetimes

Having established the importance of magnetism to calculate phonon frequencies even above T_N , we now discuss its possible effects on the linewidths. As we have seen, the FWHM exhibits a singular behavior, with a marked jump across T_N for modes A_g-2 and A_g-3 . This behavior is strongly reminiscent of that of the magnetization but also of that of the electrical resistivity $\rho(T)$ reported in Refs. [14,17]. Interestingly, we note that this empirical relationship between $\rho(T)$ and the line shape of Raman-active phonons can be seen in

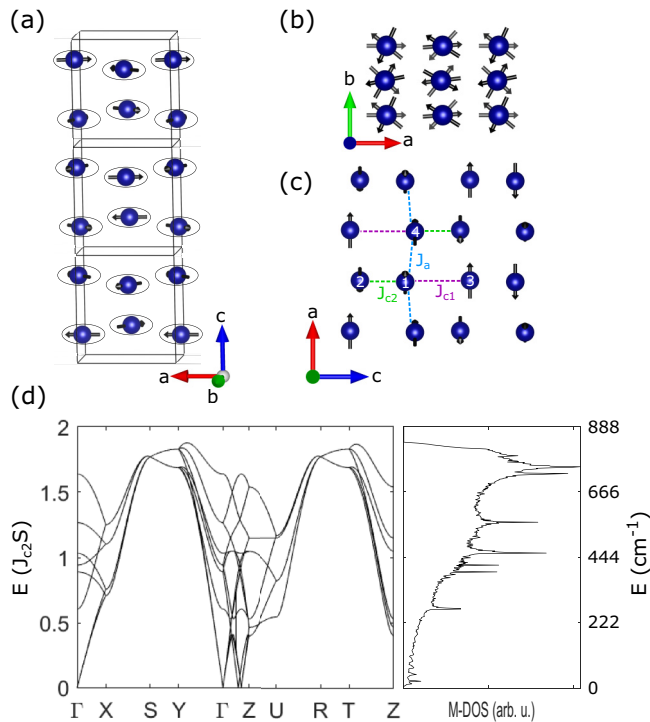


FIG. 7. (a) The double helical magnetic ground state of CrAs with the propagation vector of $Q_z = 0.36 \times 2\pi c^*$. (b) A view of the magnetic structure along the c axis. (c) Magnetic exchange couplings that are required to stabilize such a magnetic ground state are marked on the crystallographic ac plane of CrAs. (d) Left: Magnon dispersion along high-symmetry directions in reciprocal space. Right: Magnon density of states (M-DOS). J_{c2} and S in energy units are the strongest exchange coupling and the spin state of Cr, respectively. According to the estimation of $2J_{c2}S \approx 110$ meV from inelastic neutron-scattering data [17], an additional energy scale is given in cm^{-1} for M-DOS.

other magnetic metals, in particular, in the parent compounds of Fe-based superconductors such as BaFe_2As_2 [37]. There, it has qualitatively been understood in terms of reduction of the electron-phonon interaction caused by the opening of a spin-density-wave gap in the electronic density of states. In this context, further investigation on changes in the electronic structure of CrAs across T_N , as well as subsequent studies on P-doped CrAs (which strongly impacts $\rho(T)$ [17]) using, e.g., angle-resolved photoemission spectroscopy, would be required to better understand the origin of these linewidth anomalies).

The linewidth of the A_g-1 mode, on the other hand, exhibits a completely different temperature dependence; a cusplike shape with a maximum at ≈ 125 K [Fig. 3(e)], a temperature that does not correspond to any known anomaly in the structure or the thermodynamic properties of CrAs. This in turn suggests that such a remarkable temperature dependence of the linewidth of A_g-1 arises from a compromise between opposite effects below T_N . We already established that this mode is highly sensitive to the underlying magnetism. Therefore, spin-phonon coupling appears as a possible damping mechanism below T_N , which is then partially compensated at low temperatures by regular lattice anharmonic effects.

Notably, in the past, several studies have highlighted the impact of spin-phonon coupling on phonon frequencies (see, e.g., [38–40]), but its effect on the phonon linewidths has been barely discussed. Recent experimental studies on antiferromagnetic $\text{Pr}_{1-x}\text{Ca}_x\text{MnO}_3$ [41], SmCrO_3 , and GdCrO_3 [42,43] reported similar phonon broadenings below T_N and point towards a generic phenomenology for which a robust theoretical framework is missing to date.

C. Magnetic Raman scattering

The excitations at around 350 and 1700 cm^{-1} are only detected below T_N and in the absence of broken translational symmetry, so that they are very likely to have magnetic origin. Single magnon Raman scattering arises from magnetic anisotropies (that gap the magnon spectra at the zone center) and generally gives rise to sharp low-energy Raman features [44–46] in long-range magnetically ordered systems such as CrAs. In contrast, two-magnon Raman scattering generally results in broader features [44,47,48]. The large FWHMs of the excitations lead us to suspect their two-magnon origin. As the two-magnon Raman scattering process must fulfill the momentum conservation law and result in a $q \approx 0$ excitation, it must correspond to the excitation of two magnons with opposite momenta. Those primarily involve regions of the reciprocal space with large magnon density of states (M-DOS), i.e., zone boundaries [49], corresponding to local spin flips in a real-space picture.

In the past, measurements of the two-magnon Raman spectra correctly estimated the exchange coupling constant of the parent compound of high- T_c cuprates [47], which are $S = 1/2$ antiferromagnets on square lattices. The more general case of a noncollinear magnet presented here is unfortunately more complicated to interpret. The two-magnon energy can be evaluated, in principle, in two ways. We can either calculate the energy cost of two neighboring spin flips or compute the M-DOS. However, in both cases, difficulties arise from the noncollinearity and the itinerant character of the system, when, e.g., considering final-state interactions [50]. Additionally, neither the actual spin contribution to the total magnetic moment ($1.73 \mu_B/\text{Cr}$ [8]) nor the exchange coupling constants are precisely known. Regarding the spin value, the large ($\sim 60\%$) orbital contribution to the total magnetic moment of metallic Cr [51] strongly suggests that the spin in CrAs might be larger than $1/2$.

The magnetic structure of CrAs has been previously [7,17] modeled using a Heisenberg-like Hamiltonian $\mathcal{H} = \sum_{i,j} J_{ij} \tilde{S}_i \cdot \tilde{S}_j$ considering the predominant exchange couplings, which are denoted as J_a , J_b , J_{c1} , and J_{c2} following [17] [shown in Fig. 7(a)]. The stability conditions for the double helical magnetic ground state have been determined as $J_{c2}/J_a = 7.1$ and $J_{c1}/J_a = -0.52$ [7], irrespective of the value and sign of J_b [52]. However, the values of the exchange couplings have been estimated only from inelastic neutron-scattering data on polycrystalline samples [17], assuming that the total magnetic excitation bandwidth of ~ 110 meV is dominated by $J_{c2} \gg J_{c1}$, J_a and amounts to $\sim 2J_{c2}S$.

Based on these estimated exchange parameters, we have calculated the linear spin-wave spectra [53] of CrAs and M-DOS as shown in Fig. 7(d) in units of $J_{c2}S$. The latter is clearly

dominated by the highest energy excitations around $\sim 1.7J_{c2}S$, which amounts to 93.5 meV (754cm^{-1}) according to the estimate of Ref. [17]. Considering two-magnon processes and doubling this value (187 meV or 1508 cm^{-1}), we obtain an energy relatively close to that of the feature at $1700\text{ cm}^{-1} \approx 211\text{ meV}$. In this case, however, none of the other features of this M-DOS can be easily associated with the 350-cm^{-1} mode.

This highlights the fact that linear spin-wave theory is not appropriate to discuss the magnetic excitation spectra of noncollinear magnets. As pointed out in Ref. [54], nontrivial anharmonic corrections to the spin-wave spectrum for a noncollinear magnet appear already to the first order in $1/S$ and strongly modify the spin-wave dispersion. This has, for instance, been recently verified experimentally in noncollinear antiferromagnetic CaCr_2O_4 [55], in which the magnetic excitations are found to be much softer than the predictions from the linear spin-wave theory. Thus these call for experimental investigation of the dispersion of the magnetic excitations in CrAs.

We note that though the magnetic Raman response of $\text{Cd}_2\text{Os}_2\text{O}_7$ shows a good agreement with its M-DOS [56], difficulties have been encountered in interpreting the two-magnon Raman data of other noncollinear magnets such as $\alpha\text{-SrCr}_2\text{O}_4$ [57] or $\text{Bi}_2\text{Fe}_4\text{O}_9$ [58]. To the best of our knowledge, the impact of these effects on the magnetic Raman response have been evaluated only for the case of a triangular lattice [59,60]. However, they are strongly model dependent and should be evaluated for the specific magnetic structure of CrAs. The present experimental results will provide a strong benchmark for future experimental and theoretical investigations.

VI. SUMMARY AND CONCLUSION

In summary, we have reported a detailed Raman scattering study of lattice and magnetic excitations as functions of temperature in CrAs single crystals. We detected abrupt changes in phonon frequency for all A_g modes across $T_N = 265\text{ K}$, at which CrAs undergoes a first-order magnetostructural phase transition characterized by the formation of a double helical magnetic structure, which is accompanied by a large expansion of the crystal unit cell. We further reported evidences of magnetic light scattering in this itinerant noncollinear magnet.

First-principles lattice structure and dynamics calculations (constrained to the experimental lattice parameters) show a very good agreement with the data, particularly when magnetic order is considered. This indicates a sizeable spin-phonon coupling in CrAs, but further work is required to really quantify these effects, as we are limited to collinear magnetic structures.

Furthermore, calculations beyond the harmonic level are needed to understand the temperature dependence of the linewidth of the strongest A_g mode, which appears highly anomalous. It shows an unusual broadening in the magnetic phase down to 125 K , which might arise from its coupling to magnetic degrees of freedom. To discuss the potential relevance of these effects to superconductivity, it would be insightful to track the phonon anomalies and the magnetic

TABLE I. Structural parameters of CrAs determined from temperature-dependent single-crystal x-ray diffraction. The structure was refined in the orthorhombic space group $Pnma$. Cr as well as As reside on Wyckoff positions $4c$ with coordinates $x, \frac{1}{4}, z$. The U_{ii} denote the atomic displacement factors ($U_{12}[\text{Cr}] = U_{23}[\text{Cr}] = U_{12}[\text{As}] = U_{23}[\text{As}] = 0$). Refinement of the site occupancy factor (SOF) of Cr shows that the sample is stoichiometric within the error bars (the SOF of As was fixed to 1).

		295 (K)	$T = 95$ (K)
	a (Å)	5.6535(5)	5.6095(6)
	b (Å)	3.4737(4)	3.5905(5)
	c (Å)	6.2042(6)	6.1384(6)
Cr	x	0.0064(2)	0.0073(2)
	z	0.2012(1)	0.2056(1)
	U_{11} (Å ²)	0.0048(5)	0.0024(4)
	U_{22} (Å ²)	0.0107(5)	0.0052(5)
	U_{33} (Å ²)	0.0064(5)	0.0044(4)
	U_{13} (Å ²)	0.0001(3)	-0.0004(3)
	U_{eq} (Å ²)	0.0073(3)	0.0040(2)
	SOF	0.9988(55)	0.9984(52)
As	x	0.2022(1)	0.2054(1)
	z	0.5770(1)	0.5836(1)
	U_{11} (Å ²)	0.0075(3)	0.0048(3)
	U_{22} (Å ²)	0.0076(3)	0.0026(3)
	U_{33} (Å ²)	0.0075(3)	0.0028(3)
	U_{13} (Å ²)	0.0010(3)	0.0004(2)
	U_{eq} (Å ²)	0.0075(2)	0.0034(2)
	wR_2	4.15	3.98
	R_1	1.90	1.66

excitations as a function of hydrostatic pressure or doping (e.g., $\text{CrAs}_{1-x}\text{P}_x$) as the magnetic order is suppressed.

ACKNOWLEDGMENTS

We acknowledge C. Bernhard, R. Eder, M. Garst, C. Meingast, I. Paul, J. Schmalian, Q. Si, and S-M. Souliou for valuable discussions. The contribution from M.M. was supported by the Karlsruhe Nano Micro Facility (KNMF). K.W. acknowledges funding from the Alexander von Humboldt Foundation.

APPENDIX A: EXPERIMENTAL STRUCTURAL PARAMETERS AT 295 AND 95 K

Table I summarizes the structural parameters of CrAs single crystals at 295 and 95 K. The detail procedure to obtain such parameters is mentioned in Sec. II A.

APPENDIX B: RAMAN SPECTRA IN CROSSED POLARIZATION

The high-resolution Raman spectra in crossed-polarization configuration are extremely weak (not shown), in which the

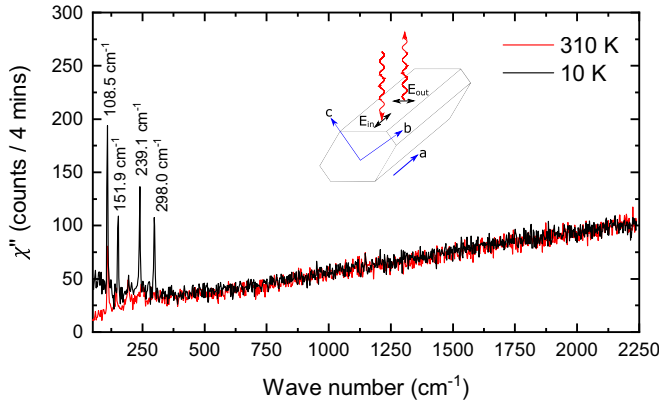


FIG. 8. Low-resolution Raman spectra in crossed-polarization geometry at 10 and 310 K. The incoming photon polarization was parallel to the crystallographic a axis. This polarization geometry probes phonon modes of B_{1g} and B_{2g} symmetries. No magnetic scattering is visible in this polarization geometry. Inset schematically shows the polarization geometry with respect to the corresponding crystal facet, in which incoming (E_{in}) and outgoing (E_{out}) polarizations are marked.

incoming photon polarization is parallel to the crystallographic a axis of the crystal. The intensity I of the strongest mode in this configuration amounts to $I = 0.2$ counts/s at 225 K, whereas at the same temperature, the strongest A_g phonon in parallel polarization has $I = 5$ counts/s.

However, we could resolve at least four phonon modes of B_{1g} and B_{2g} symmetry in the Raman spectra measured with the low-resolution grating at 10 and 310 K, as shown in Fig. 8. We did not observe any magnetic Raman scattering in this configuration.

APPENDIX C: RAMAN SPECTRA FROM THE SIX FACETS OF A CrAs CRYSTAL

Figure 9 shows the Raman spectra in XX geometry, which were obtained from the six facets of a physical CrAs crystal. In good agreement with the relevant polarization selection rules, we always observed only A_g modes, irrespective of the direction of the incoming photons.

APPENDIX D: ANALYSIS OF FLEURY-LOUDON HAMILTONIAN

The effective two-magnon light-scattering operator can be written as

$$\hat{O} = \sum_{i,j} \eta_{ij} (\vec{E}_i \cdot \vec{d}_{ij}) (\vec{E}_s \cdot \vec{d}_{ij}) \vec{S}_i \cdot \vec{S}_j,$$

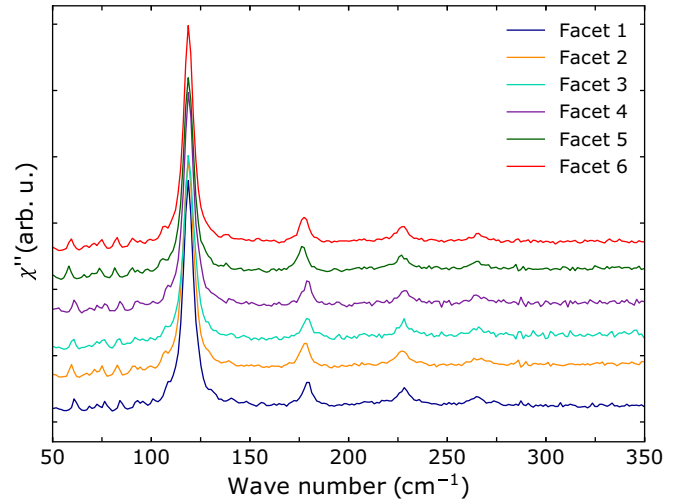


FIG. 9. Raman spectra in XX geometry at room temperature from the six facets of a CrAs crystal.

where \vec{E}_i (\vec{E}_s) is the polarization of the incident (scattered) light, \vec{d}_{ij} is the unit vector connecting the magnetic sites i and j , on which the spins \vec{S}_i and \vec{S}_j , respectively, sit, and η_{ij} is a matrix element proportional to the exchange coupling constant [61]. The sum runs over all pairs of magnetic atoms. The relevant magnetic sites are marked in Fig. 7(c). The angle between \vec{E}_{in} (parallel to the a axis) and Cr1-Cr2 or Cr1-C3 is very close to 90° . Thus we can neglect the projections of \vec{d}_{12} and \vec{d}_{13} vectors on the crystallographic a axis. In the chosen scattering geometry, the main contribution arises from scattering across the Cr1-Cr4 bond (\vec{d}_{14}).

For the XX geometry, we get

$$\hat{O}_{XX} \sim \eta_{14} \cos^2(\theta_{14}) \vec{S}_1 \cdot \vec{S}_4,$$

where θ_{14} ($\approx 11^\circ$) is the angle between the a axis and \vec{d}_{14} . For the XY geometry, we obtain

$$\hat{O}_{XY} \sim \eta_{14} \cos(\theta_{14}) \sin(\theta_{14}) \cos^2(\alpha) \vec{S}_1 \cdot \vec{S}_4,$$

in which $\alpha \approx 30^\circ$, since the orientation of the measured facet is (011).

The ratio between the magnetic scattering intensities of the two channels will therefore be

$$\frac{I_{XY}}{I_{XX}} \sim |\tan(\theta_{14}) \cos^2(\alpha)|^2 \sim 2 \times 10^{-2}.$$

Such a ratio is consistent with the absence of a magnetic scattering signal in the XY geometry.

[1] Y. Kamihara, T. Watanabe, M. Hirano, and H. Hosono, *J. Am. Chem. Soc.* **130**, 3296 (2008).
 [2] M. Rotter, M. Tegel, and D. Johrendt, *Phys. Rev. Lett.* **101**, 107006 (2008).
 [3] F.-C. Hsu, J.-Y. Luo, K.-W. Yeh, T.-K. Chen, T.-W. Huang, P. M. Wu, Y.-C. Lee, Y.-L. Huang, Y.-Y. Chu, D.-C. Yan, and M.-K. Wu, *Proc. Natl. Acad. Sci. USA* **105**, 14262 (2008).

[4] X. C. Wang, Q. Q. Liu, Y. X. Lv, W. B. Gao, L. X. Yang, R. C. Yu, F. Y. Li, and C. Q. Jin, *Solid State Commun.* **148**, 538 (2008).
 [5] H. Wada and Y. Tanabe, *Appl. Phys. Lett.* **79**, 3302 (2001).
 [6] K. Selte, A. Kjekshus, W. E. Jamison, A. F. Andresen, J. E. Engebretsen, and L. Ehrenberg, *Acta Chem. Scand.* **25**, 1703 (1971).

- [7] A. Kallel, H. Boller, and E. F. Bertaut, *J. Phys. Chem. Solids* **35**, 1139 (1974).
- [8] L. Keller, J. S. White, M. Frontzek, P. Babkevich, M. A. Susner, Z. C. Sims, A. S. Sefat, H. M. Rønnow, and C. Rüegg, *Phys. Rev. B* **91**, 020409 (2015).
- [9] H. Watanabe, N. Kazama, Y. Yamaguchi, and M. Ohashi, *J. Appl. Phys.* **40**, 1128 (1969).
- [10] T. Suzuki and H. Ido, *J. Appl. Phys.* **73**, 5686 (1993).
- [11] H. Boller and A. Kallel, *Solid State Commun.* **9**, 1699 (1971).
- [12] R. Blachnik, G. Kuderma, F. Grønvoold, A. Alles, B. Falk, and E. F. Westrum, *J. Chem. Thermodyn.* **10**, 507 (1978).
- [13] H. Kotegawa, S. Nakahara, H. Tou, and H. Sugawara, *J. Phys. Soc. Japan* **83**, 093702 (2014).
- [14] W. Wu, J. Cheng, K. Matsubayashi, P. Kong, F. Lin, C. Jin, N. Wang, Y. Uwatoko, and J. Luo, *Nat. Commun.* **5**, 5508 (2014).
- [15] Y. Shen, Q. Wang, Y. Hao, B. Pan, Y. Feng, Q. Huang, L. W. Harriger, J. B. Leao, Y. Zhao, R. M. Chisnell, J. W. Lynn, H. Cao, J. Hu, and J. Zhao, *Phys. Rev. B* **93**, 060503 (2016).
- [16] W. Wu, X. Zhang, Z. Yin, P. Zheng, N. Wang, and J. Luo, *Sci. China: Phys., Mech. Astron.* **53**, 1207 (2010).
- [17] M. Matsuda, F. K. Lin, R. Yu, J.-G. Cheng, W. Wu, J. P. Sun, J. H. Zhang, P. J. Sun, K. Matsubayashi, T. Miyake, T. Kato, J.-Q. Yan, M. B. Stone, Q. Si, J. L. Luo, and Y. Uwatoko, *Phys. Rev. X* **8**, 031017 (2018).
- [18] A. Nigro, P. Marra, C. Autieri, W. Wu, J. Cheng, J. Luo, and C. Noce, *Europhys. Lett.* **125**, 57002 (2019).
- [19] Q. Niu, W. C. Yu, K. Y. Yip, Z. L. Lim, H. Kotegawa, E. Matsuoka, H. Sugawara, H. Tou, Y. Yanase, and S. K. Goh, *Nat. Commun.* **8**, 15358 (2017).
- [20] H. Kotegawa, S. Nakahara, R. Akamatsu, H. Tou, H. Sugawara, and H. Harima, *Phys. Rev. Lett.* **114**, 117002 (2015).
- [21] T. P. Devereaux and R. Hackl, *Rev. Mod. Phys.* **79**, 175 (2007).
- [22] T. Suzuki and H. Ido, *J. Appl. Phys.* **55**, 2042 (1984).
- [23] G. M. Sheldrick, *Acta Crystallogr., Sect. A: Found. Crystallogr.* **64**, 112 (2008).
- [24] V. Petříček, M. Dušek, and L. Palatinus, *Z. Kristallogr. - Cryst. Mater.* **229**, 345 (2014).
- [25] M. I. Aroyo, J. M. Perez-Mato, D. Orobengoa, E. Tasci, G. De La Flor, and A. Kirov, *Bulg. Chem. Commun.* **43**, 183 (2011).
- [26] M. I. Aroyo, A. Kirov, C. Capillas, J. M. Perez-Mato, and H. Wondratschek, *Acta Crystallogr., Sect. A: Found. Crystallogr.* **62**, 115 (2006).
- [27] S. G. Louie, K.-M. Ho, and M. L. Cohen, *Phys. Rev. B* **19**, 1774 (1979).
- [28] J. P. Perdew, K. Burke, and M. Ernzerhof, *Phys. Rev. Lett.* **77**, 3865 (1996).
- [29] R. Heid and K. P. Bohnen, *Phys. Rev. B* **60**, R3709 (1999).
- [30] P. G. Klemens, *Phys. Rev.* **148**, 845 (1966).
- [31] J. Menéndez and M. Cardona, *Phys. Rev. B* **29**, 2051 (1984).
- [32] N. W. Ashcroft and N. D. Mermin, *Solid State Physics* (Harcourt College Publishers, Philadelphia, PA, 1976).
- [33] C. Autieri and C. Noce, *Philos. Mag.* **97**, 3276 (2017).
- [34] D. Reznik, K. Lokshin, D. C. Mitchell, D. Parshall, W. Dmowski, D. Lamago, R. Heid, K.-P. Bohnen, A. S. Sefat, M. A. McGuire, B. C. Sales, D. G. Mandrus, A. Subedi, D. J. Singh, A. Alatas, M. H. Upton, A. H. Said, A. Cunsolo, Y. Shvyd'ko, and T. Egami, *Phys. Rev. B* **80**, 214534 (2009).
- [35] T. Yildirim, *Physica C* **469**, 425 (2009).
- [36] J. Łażewski, P. Piekarczyk, J. Toboła, B. Wiendlocha, P. T. Jochym, M. Sternik, and K. Parlinski, *Phys. Rev. Lett.* **104**, 147205 (2010).
- [37] M. Rahlenbeck, G. L. Sun, D. L. Sun, C. T. Lin, B. Keimer, and C. Ulrich, *Phys. Rev. B* **80**, 064509 (2009).
- [38] E. Granado, A. Garcia, J. Sanjurjo, C. Rettori, I. Torriani, E. Prado, R. Sanchez, A. Canerio, and S. Oseroff, *Phys. Rev. B* **60**, 11879 (1999).
- [39] S. Issing, A. Pimenov, V. Y. Ivanov, A. A. Mukhin, and J. Geurts, *Phys. Rev. B* **81**, 024304 (2010).
- [40] J. Laverdière, S. Jandl, A. A. Mukhin, V. Y. Ivanov, V. G. Ivanov, and M. N. Iliev, *Phys. Rev. B* **73**, 214301 (2006).
- [41] R. Gupta, G. V. Pai, A. K. Sood, T. V. Ramakrishnan, and C. N. R. Rao, *Europhys. Lett.* **58**, 778 (2002).
- [42] M. El Amrani, M. Zaghrioui, V. Ta Phuoc, F. Gervais, and N. E. Massa, *J. Magn. Magn. Mater.* **361**, 1 (2014).
- [43] V. Srinu Bhadrani, B. Rajeswaran, A. Sundaresan, and C. Narayana, *Europhys. Lett.* **101**, 17008 (2013).
- [44] S. L. Gleason, T. Byrum, Y. Gim, A. Thaler, P. Abbamonte, G. J. MacDougall, L. W. Martin, H. D. Zhou, and S. L. Cooper, *Phys. Rev. B* **89**, 134402 (2014).
- [45] E. Meloche, M. G. Cottam, V. P. Gnezdilov, and D. J. Lockwood, *Phys. Rev. B* **81**, 024426 (2010).
- [46] H. Gretarsson, J. Saucedo, N. H. Sung, M. Höppner, M. Minola, B. J. Kim, B. Keimer, and M. Le Tacon, *Phys. Rev. B* **96**, 115138 (2017).
- [47] K. B. Lyons, P. A. Fleury, J. P. Remeika, A. S. Cooper, and T. J. Negran, *Phys. Rev. B* **37**, 2353 (1988).
- [48] H. Gretarsson, N. H. Sung, M. Höppner, B. J. Kim, B. Keimer, and M. Le Tacon, *Phys. Rev. Lett.* **116**, 136401 (2016).
- [49] P. Lemmens, G. Güntherodt, and C. Gros, *Phys. Rep.* **375**, 1 (2003).
- [50] C. M. Canali and S. M. Girvin, *Phys. Rev. B* **45**, 7127 (1992).
- [51] E. Fawcett, *Rev. Mod. Phys.* **60**, 209 (1988).
- [52] Using the ratio of Cr-Cr distances along the a and b axis, we approximate that $J_b \approx J_a/1.26$.
- [53] S. Toth and B. Lake, *J. Phys.: Condens. Matter* **27**, 166002 (2015).
- [54] A. V. Chubukov, *Zh. Eksp. Teor. Fiz.* **85**, 1319 (1983) [*Sov. Phys. JETP* **58**, 765 (1983)].
- [55] D. Wulferding, K.-Y. Choi, P. Lemmens, A. N. Ponomaryov, J. van Tol, A. T. M. Nazmul Islam, S. Toth, and B. Lake, *J. Phys.: Condens. Matter* **24**, 435604 (2012).
- [56] T. M. H. Nguyen, L. J. Sandilands, C. H. Sohn, C. H. Kim, A. L. Wysocki, I.-S. Yang, S. J. Moon, J.-H. Ko, J. Yamaura, Z. Hiroi, and T. W. Noh, *Nat. Commun.* **8**, 251 (2017).
- [57] M. E. Valentine, S. Koohpayeh, M. Mourigal, T. M. McQueen, C. Broholm, N. Drichko, S. E. Dutton, R. J. Cava, T. Birol, H. Das, and C. J. Fennie, *Phys. Rev. B* **91**, 144411 (2015).
- [58] M. N. Iliev, A. P. Litvinchuk, V. G. Hadjiev, M. M. Gospodinov, V. Skumryev, and E. Ressouche, *Phys. Rev. B* **81**, 024302 (2010).
- [59] N. Perkins and W. Brenig, *Phys. Rev. B* **77**, 174412 (2008).
- [60] N. B. Perkins, G.-W. Chern, and W. Brenig, *Phys. Rev. B* **87**, 174423 (2013).
- [61] C.-C. Chen, C. J. Jia, A. F. Kemper, R. R. P. Singh, and T. P. Devereaux, *Phys. Rev. Lett.* **106**, 067002 (2011).